The Astrophysical Journal, 844:67 (14pp), 2017 July 20 https://doi.org/10.3847/1538-4357/aa784a

The Double Galaxy Cluster A2465. III. X-Ray and Weak-lensing Observations*

Gary A. Wegner[1], Keiichi Umetsu[2], Sandor M. Molnar[2], Mario Nonino[3], Elinor Medezinski[4], Felipe Andrade-Santos[5], Akos Bogdan[5], Lorenzo Lovisari[5], William R. Forman[5], and Christine Jones[5]
[1] Department of Physics & Astronomy, 6127 Wilder Laboratory, Hanover, NH 03745, USA; gary.wegner@dartmouth.edu
[2] Institute of Astronomy and Astrophysics, Academia Sinica, P.O. Box 23-141, Taipei 10617, Taiwan
[3] INAF/Osservatorio Astronomico di Trieste, via G. B. Tiepolo 11, 34143 Trieste, Italy
[4] Department of Astrophysical Sciences, 4 Ivy Lane, Princeton, NJ 08544, USA
[5] Harvard-Smithsonian Center for Astrophysics, 60 Garden Street, Cambridge, MA 02138, USA
Received 2016 December 22; revised 2017 June 2; accepted 2017 June 5; published 2017 July 24

Abstract

We report *Chandra* X-ray observations and optical weak-lensing measurements from Subaru/Suprime-Cam images of the double galaxy cluster A2465 ($z = 0.245$). The X-ray brightness data are fit to a β model to obtain the radial gas density profiles of the northeast (NE) and southwest (SW) subcomponents, which are seen to differ in structure. We determine core radii, central temperatures, the gas masses within r_{500c}, and the total masses for the broader NE and sharper SW components assuming hydrostatic equilibrium. There is no large X-ray excess between the two components. The central entropy of the NE subcluster is about two times higher than the SW. Along with its structural properties and an apparent radio halo that is a sign of a merger, this suggests that the NE component has undergone merging on its own. The weak-lensing analysis gives virial masses for each substructure, which compare well with earlier dynamical results. The derived outer mass contours of the SW subcomponent from weak lensing are more irregular and extended than those of the NE. Although there is a weak enhancement and small offsets between X-ray gas and mass centers from weak lensing, the lack of large amounts of gas between the two subclusters indicates that A2465 is in a pre-merger state. We discuss star formation enhancement in this system resulting from its dynamics and shock-induced star formation scenarios. A dynamical model that is consistent with the observed cluster data, based on the FLASH program and the radial infall model, is constructed, where the subclusters currently separated by $\sim$1.2 Mpc are approaching each other at $\sim$2000 km s^{-1} and will meet in $\sim$0.4 Gyr.

Key words: dark matter – galaxies: clusters: general – galaxies: clusters: individual (Abell 2465) – gravitational lensing: weak – X-rays: galaxies: clusters

1. Introduction

In the Λ cold dark matter (ΛCDM) picture of large-scale structure formation, galaxy clusters grow hierarchically from smaller knots of higher density, forming and merging along the intersection of filaments. At present, several double or multiple galaxy clusters in different stages of merging are known. Examples of interacting clusters that have undergone merging interactions include, e.g., the "Bullet" (Clowe et al. 2006), RXJ1347.5-1145 (Bradač et al. 2008b), MACSJ0025.4-1222 (Bradač et al. 2008a), A2744 (Owers et al. 2011), A2146 (Russell et al. 2012), and DLSCL J00916.2+2915 (Dawson et al. 2012). Some examples of pre-collisional binary clusters include A3716 (Andrade-Santos et al. 2015) and A1750 and A1758 (Okabe & Umetsu 2008; Hwang & Lee 2009; Molnar et al. 2013).

Investigating double galaxy clusters by combining optical, radio, and X-ray data with gravitational lensing provides insight into the behavior of the matter components, the star formation, the evolution of of these clusters, and ultimately large-scale structure. Weak lensing is a powerful tool for reconstructing full cluster mass distributions on large angular scales and for identifying mass sub-structures (Okabe & Umetsu 2008; Medezinski et al. 2013; Umetsu et al. 2012). In X-rays, the baryonic gas can be compared with the collisionless galaxy and dark matter components. The observed shapes of the sub-structures can range from circular symmetry, indicating relaxed systems, to objects with separated dark and baryonic matter and disturbed gas, indicating core-crossing events spanning pre- to post-mergers (e.g., Markevitch & Vikhlinin 2007).

Modeling cluster collisions probes the different behavior of the collisionless dark matter and baryonic gas constituents (e.g., Roettiger et al. 1997; Takizawa 2000; Ricker & Sarazin 2001; Poole et al. 2006; Molnar et al. 2012). Several investigators (e.g., Spergel & Steinhardt 2000; Randall et al. 2008; Kahlhoefer et al. 2014) have proposed utilizing these effects to study non-gravitational interactions in the collisions of the galaxy clusters to gain information on the properties of the dark matter component. Vijayaragharan & Ricker (2013) showed that the separation of the baryonic and collisionless dark matter begins to be felt even in the pre-merger phases, so details of the dynamics at all stages of cluster mergers provide information about the physical interplay between dark matter and baryons.

In addition, non-gravitational evolution, such as varying enhancements of star formation, are important (e.g., Wegner et al. 2015; Stroe et al. 2015a, 2015b; Sobral et al. 2015). Not every system shows these effects, which could depend on several factors, e.g., on the dynamics of the interaction and formation history. Massive "hot" clusters seem to have less star formation than "cold" less massive clusters (Laganá et al. 2008). It is thus interesting to compare star formation in pre- and post-merger galaxy clusters as a possible indicator of

* Based in part on data collected at the Subaru Telescope, which is operated by the National Astronomical Society of Japan.

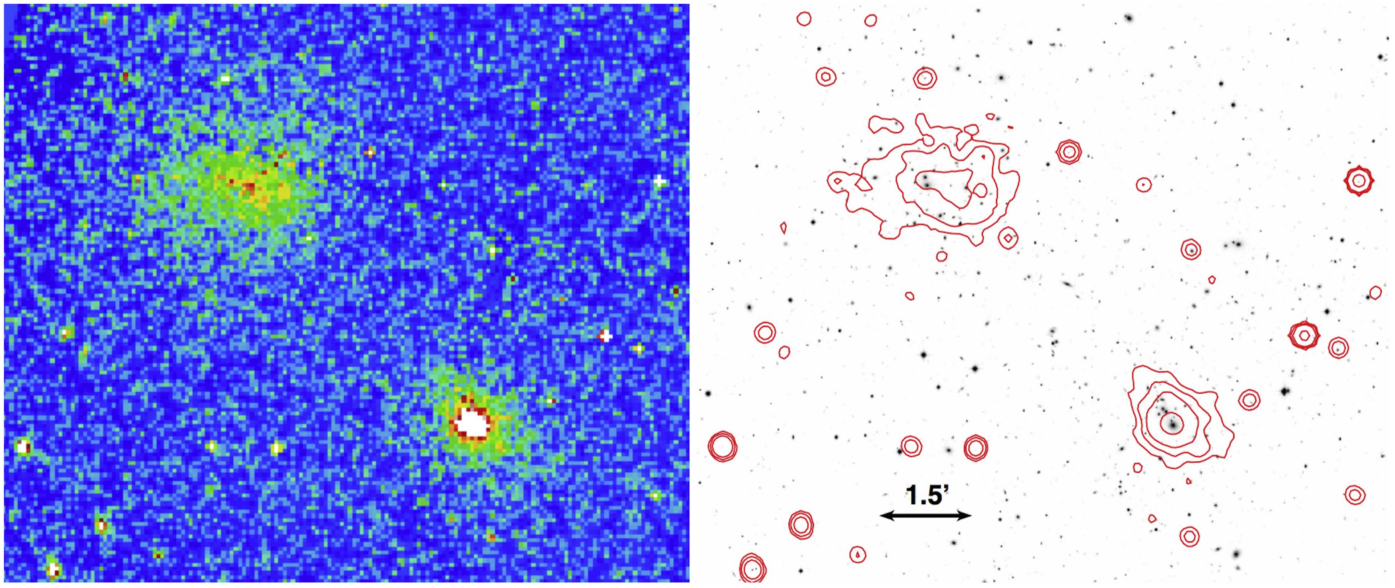

Figure 1. Left: *Chandra* image of A2465 in the 0.5 to 3.0 keV energy band with 8 pixel binning. Right: CFHT megaprime i' image with the isodensity X-ray contours. North is to the top and west to the right. The images are approximately 11 × 9 arcmin^2. The NE component is to the upper left and comparison with the SW component shows the differences in their structures. The X-ray center of the NE subcluster is slightly displaced from its central BCGs while the SW X-ray peak is nearly centered on the BCG.

galaxy evolution mechanisms and their connection with dynamics and dark matter. In many cases, the substructure of galaxy clusters complicates their interpretation if they have many components (e.g., Merten et al. 2011; Cohen et al. 2014; Medezinski et al. 2016). Consequently finding simple clearly double structures is valuable for elucidating the dynamics of their components.

A2465, the subject of this paper, appears to be a well-defined double cluster system undergoing a major merger. First reported by Abell (1958) as a modest Richness Class 1 cluster, its double nature was not known until Vikhlinin et al. (1998) gave *ROSAT* X-ray fluxes of the two subcomponents, referred to in this paper as the northeast (NE) and southwest (SW) components (See Figure 1). Perlman et al. (2002) found redshifts of $z = 0.245$ for both, establishing their physical relationship. The NE component of the cluster is detected as a 1.4 Ghz source (Condon et al. 1998; Helfand et al. 2015).

The optical properties of A2465 have been described in Wegner (2011; Paper I) and Wegner et al. (2015; Paper II). Virial masses $M_{\rm vir} = (4.1 \pm 0.8) \times 10^{14}\,M_\odot$ and $(3.8 \pm 0.8) \times 10^{14}\,M_\odot$ for the NE and SW components, respectively, were derived from optical velocity dispersions. In Paper II, it was found that star formation rates (SFRs) of member galaxies appear enhanced. Although they have similar masses, the two subclusters differ in their radial profiles. The NE is less compact, while the SW is the less massive and smaller in extent with a brighter inner core. Since the projected separation between the two subclusters is 1.2 Mpc and their optical halo radii are $r_{200c} \approx 1.2$ and 1.25 Mpc (Paper I), detectable effects of their interaction seem possible.

To look for such effects, we obtain and analyze new *Chandra* X-ray observations and weak-lensing measurements from Subaru Suprime-Cam imaging. These are utilized to determine the state of the baryonic gas and measure the structures and mass distributions of the double components of A2465, study their interaction, and settle whether they are pre- or post-core crossing.

This paper is arranged as follows. Section 2 discusses the X-ray data, Section 2.1 presents the *Chandra* observations and reductions, and Section 2.2 discusses the optical appearances of the centers of the subcomponents. Section 2.3 analyzes the X-ray spatial and spectral data and the resulting total and gas masses for the NE and SW subclusters. Section 2.4 determines the gas temperatures of the sub-structures. Section 2.5 describes the search for gas between the subclusters and Section 2.6 derives the individual entropies. Section 3 contains the optical imaging data and weak-lensing results for A2465. Section 3.1 covers the observations, while Sections 3.2 and 3.3 explain the shape measurements and background selection for the weak-lensing analysis, and multi-halo mass modeling is in Section 3.4. Section 4 concerns the dynamical state and the modeling of A2465. Section 5 discusses these results and how the cluster compares with other merging galaxy clusters. Section 6 lists our conclusions.

We assume a standard ΛCDM cosmology with $\Omega_{\rm m} = 0.3$, $\Omega_\Lambda = 0.7$, and $H_0 = 100h$ km s^{-1} Mpc^{-1} with $h = 0.7$. For the cluster's mean redshift, $z = 0.245$, the luminosity distance is $D_L = 1224$ Mpc and the scale on the sky is 230 kpc arcmin^{-1}. The two subclusters are separated by 5.25 arcmin or 1.2 Mpc.

We use the standard notation $M_{\Delta c}$ to denote the mass enclosed within a sphere of radius $r_{\Delta c}$, within which the mean overdensity is Δ_c times the critical density ρ_c of the universe at the cluster redshift. To calculate halo virial quantities, we use an expression for the virial overdensity $\Delta_{\rm vir}$ based on the spherical collapse model (see Appendix A of Kitayama & Suto 1996).

2. Properties of A2465 from X-Ray Observations

2.1. Chandra X-Ray Data

A2465 was observed 2012 October 2 and 6 in the 0.1–10 keV energy range with the ACIS-I detectors of *Chandra*, ObsIds 15547 and 14010 (PI G. A. Wegner) for 30 ks and 40 ks, respectively. Both the NE and SW subcomponents were well placed together across the instrument. With *Chandra*, about 1800

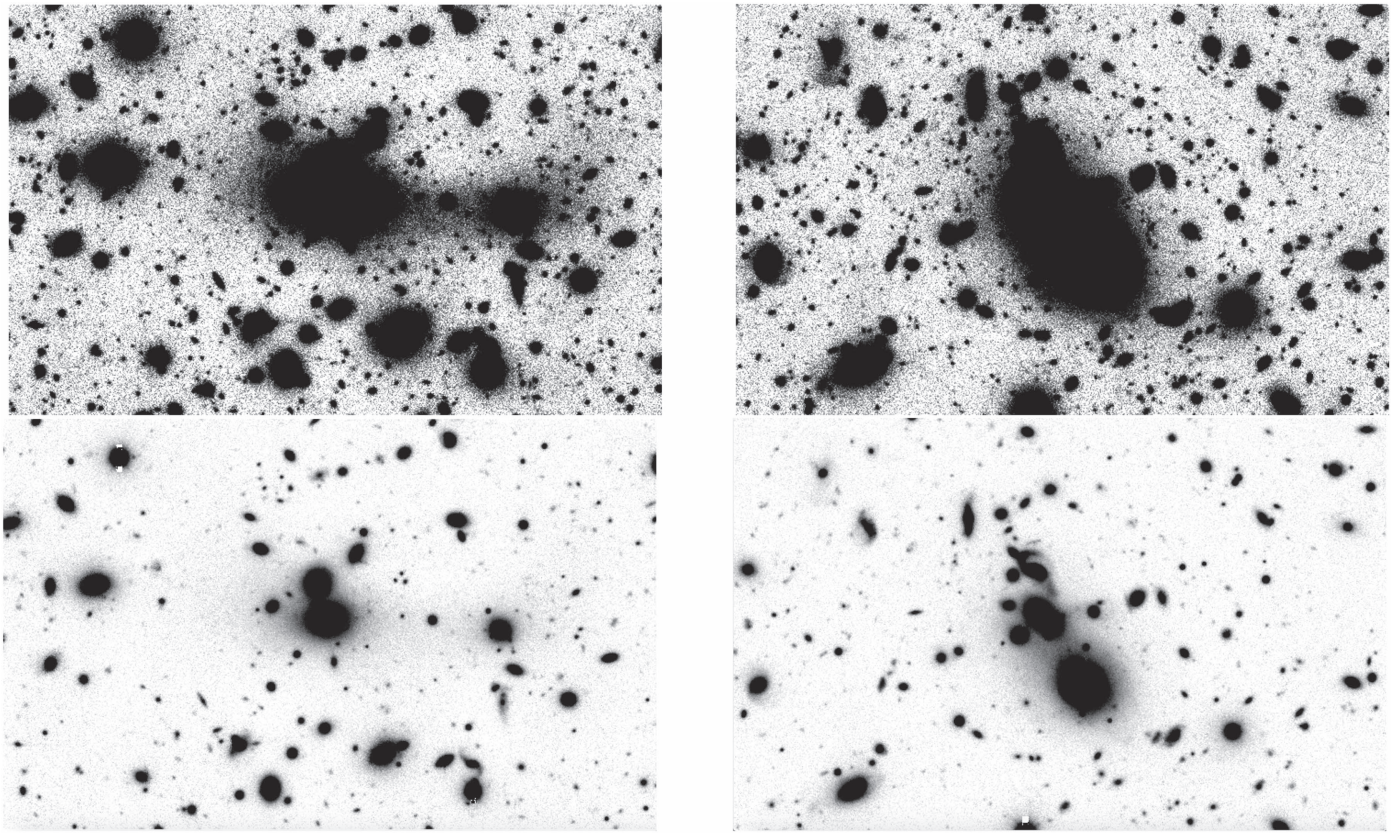

Figure 2. Centers of the subcomponents of A2465 from the combined Suprime-Cam $Vi'z'$ images described in Section 3 showing the BCGs. The NE (left) component and the SW (right) component are shown. North is to the top and west to the right. The vertical edge of each image is about 1.5 arcmin or 345 kpc. The top row shows faint details near the sky limit. The bottom row brings out the peaks of the brightest objects.

net counts were collected from each subcluster after background subtraction. Data reductions applied CALDB 4.6.7 and followed Vikhlinin et al. (2005). The reductions used the *Chandra* Interactive Analysis of Observations package and included calibration corrections to the individual photons, calibration of the spectral response, background subtraction including quiescent and soft background correction, and subtraction of the readout artifacts. We reprocessed the data, excluded flare contaminated time intervals, detected and excluded point sources, merged the data sets, utilized ACIS blank sky observations to subtract the background, and removed readout artifacts.

Although *XMM-Newton* images of A2465 are available (Paper I), we only utilize the newer *Chandra* observations. Both data sets have similar number counts, but the cluster falls at the edge of the serendipitous *XMM-Newton* field of view, which badly degrades the point-spread function and renders these data unsuitable for point source removal and producing surface brightness, emission measure, and gas mass profiles.

Figure 1 presents both the resulting *Chandra* image and its isodensity contours overlaid on the optical i' image from the 3.6 m Canada–France–Hawaii Telescope (CFHT; see Section 3.1). This shows the different appearances of the two subclusters. The X-ray profile of the NE component, although it is the more massive and luminous, has a broad central maximum. It has two X-ray concentrations oriented E and W. The SW peak is the brighter and is not near a significant radio source.

The radio properties of A2465 are discussed in Paper I. The NE X-ray peak coincides with a 6.2 mJy source in the 1.4 GHz NRAO VLA Sky Survey (NVSS; Condon et al. 1998; Helfand et al. 2015) and an optical brightest cluster galaxy (BCG). This object appears to be a radio halo, as found in merging clusters (Feretti et al. 2012). The optical BCG consists of at least three merging ellipticals and has no detected optical emission lines (Paper I and Figure 2). The NE subcluster is likely the result of a merger on its own. The SW component is more compact and shows a brighter sharp central peak. The possibility of a cool core was suggested in Paper I. The BCG in the SW subcluster also shows no optical emission lines.

2.2. Optical Appearance of the Central BCG Regions

The optical structures in the centers of the NE and SW components of A2465, which is a sum of the Subaru $Vi'z'$ images described in Section 3, is in Figure 2. In the NE clump, the light of the two central E galaxies seen in Figure 1 appears merged and connected to a third galaxy to the W and surrounded by at least three nearby E galaxies. The SW component is dominated by one large central BCG with several close smaller galaxies to the north. There are hints of arclets in each subcluster and a quadruple lens suspect can be seen as the triangle feature to the right of the NE BCG, but these are at our image limits and are outside the scope of the present paper.

2.3. The X-Ray Radial Brightness and Gas Density Profiles of A2465 NE and SW

The projected X-ray surface brightness distributions of the two components of A2465 were measured, from which the total X-ray luminosities were found to be $L_{\rm X,bol} = 9.0^{+0.3}_{-0.5} \times 10^{43}$ erg s^{-1} for the NE component and $L_{\rm X,bol} = 6.8^{+0.2}_{-0.3} \times 10^{43}$ erg s^{-1} for the SW component, comparable to the results in Paper I from

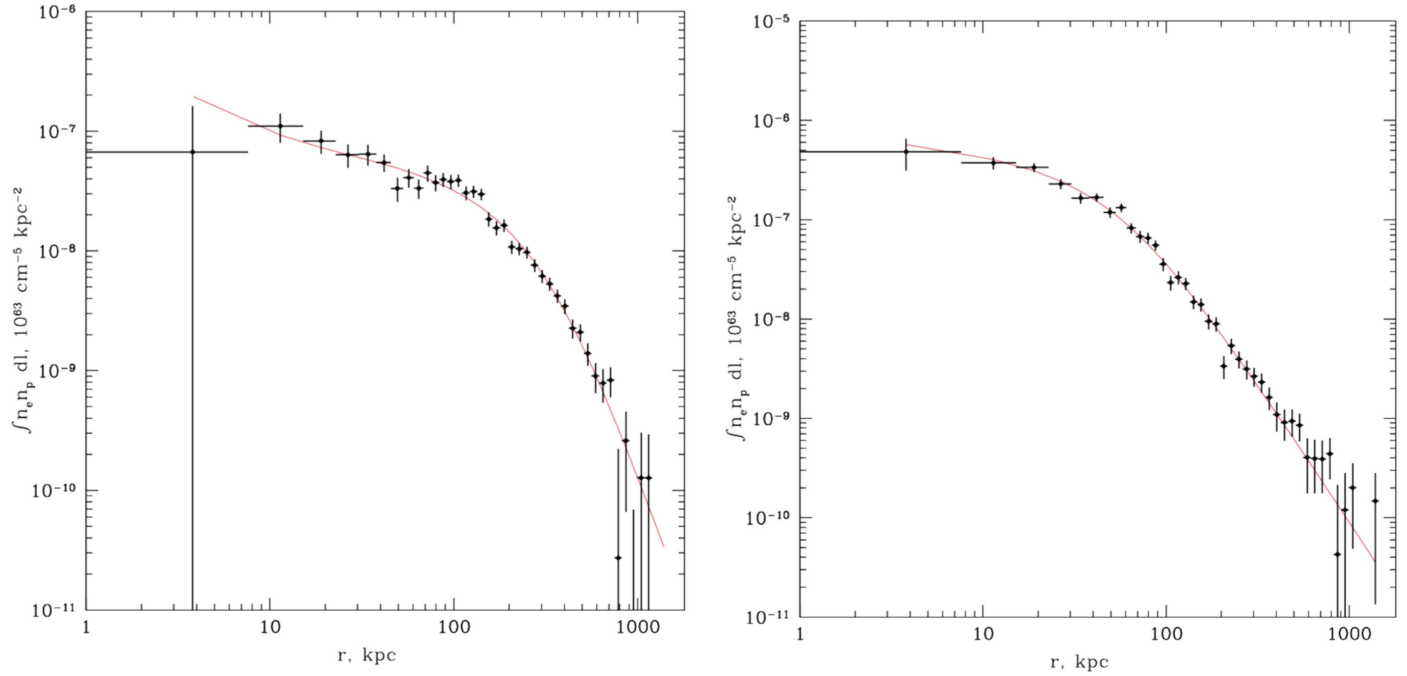

Figure 3. Emission measure profiles for the NE (left) and SW (right) subclusters of A2465 showing the *Chandra* measurements and their error bars with the resulting model fits from Equation (1).

Table 1
Chandra Emission Measure Model Best Fits (Equation (1))

Sub component	n_0 (10^{-3} cm^{-3})	r_c (kpc)	r_s (kpc)	α	β	γ	ϵ	n_{02} (cm^{-3})	r_{c2} (kpc)	β_2
A2465 NE	1.578	337	388	0.719	0.849	0.500	0.456	3.55×10^{-2}	3.37	0.502
A2465 SW	10.763	62	64	0.693	0.543	0.577	0.645	7.09×10^{-6}	2.03	0.503

XMM-Newton and *ROSAT* data. The NE L_x uncertainties do not include systematic errors as this is likely a disturbed non-axially symmetric profile.

Assuming spherical symmetry, inverting Abel's integral, yields the emission measure, ϵ_ν, from which results the particle densities, $n_p n_e = \epsilon_\nu / \Lambda(T_g)$ of each subcluster, where $\Lambda(T_g)$ describes the emissivity of the gas at temperature T_g.

The modified β model (Vikhlinin et al. 2006), which fits the emission measure profiles of a wide range of clusters was used:

$$n_p n_e = n_0^2 \frac{(r/r_c)^{-\alpha}}{[1 + (r/r_c)^2]^{3\beta-\alpha/2}} \frac{1}{[1 + (r/r_s)^\gamma]^{\epsilon/2}} + \frac{n_{02}^2}{[1 + (r^2/r_{c2})^2]^{3\beta_2}}, \quad (1)$$

where n_0 (the central number density), β, and r_c (the core radius) have their usual meanings. The additional parameters, ϵ, r_s, and γ account for a slope change and the slope width transition. A second small β profile with parameters n_{02}, r_{c2}, and β_2 is added to give extra freedom to characterize the cluster core. In the case of the NW cluster, this component gives a better fit, as n_{02} is greater than n_0. This extra component is unnecessary for the SE subcluster as n_{02} is much smaller than n_0. The resulting emission measure profiles of both subclusters and the fits to Equation (1) are shown in Figure 3. Table 1 gives the best-fit parameters for the β model for the NE and SW clumps. This confirms the visual impression of the differences between the two, where the core radius, r_c, of the NE component is nearly 5× larger than that of its SW neighbor.

The gas mass of each subcluster

$$M_g = 4\pi \int_0^{r_{500c}} \rho_g(r) r^2 dr \quad (2)$$

within r_{500c}, the spherical radius where the mean density, $\bar{\rho} = 500\rho_c$, with ρ_c as the critical density at the cluster's redshift, $z = 0.245$ was determined using (1) and Equation (4) in Andrade-Santos et al. (2015) for the central electron density, $n_{e,0}$ for a plasma with fixed electron to hydrogen density, n_e/n_H, inside a ring of given inner and outer radii, then $\rho_g = \mu_e n_e m_p$, where $\mu_e = 1.17$ is the electron mass molecular weight and $n_e/m_H = 1.2$.

The 3D gas densities and temperature profiles are used to calculate the total masses, $M_{hyd}(<r)$, inside a cluster radius, r assuming hydrostatic equilibrium, and a metal abundance for the gas of $0.3Z_\odot$,

$$M_{hyd}(<r) = -3.67 \times 10^{13} M_\odot kTr \left(\frac{d \ln \rho_g}{d \ln r} + \frac{d \ln T}{d \ln r} \right), \quad (3)$$

(e.g., Sarazin 1986; Andrade-Santos et al. 2015), where k is the Boltzmann constant, T is the gas temperature in K, and r is in megaparsecs.

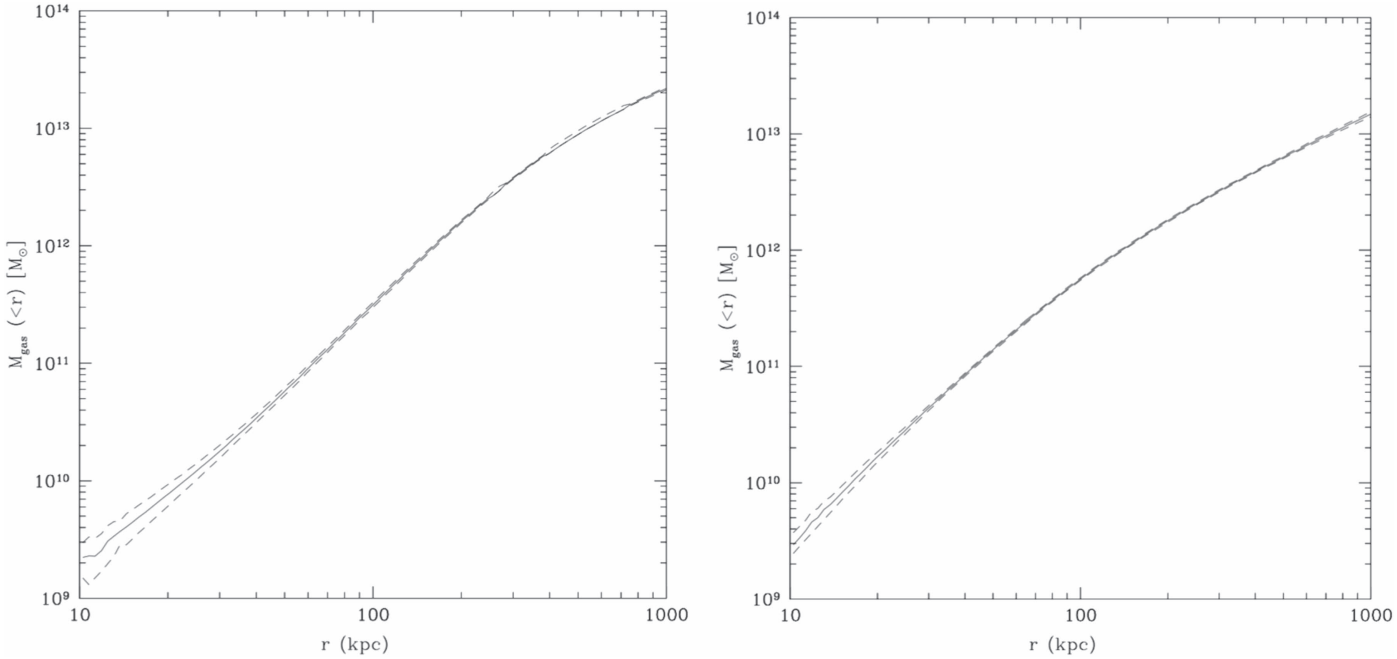

Figure 4. Enclosed gas mass $M_g(<r)$ profiles for A2465 NE (left) and SW (right). Dashed curves indicate 1σ or 68% confidence levels.

Table 2
Fitted β-model Parameters and Central Density

Sub component	r_c (kpc)	β	n_0 (10^{-3} cm^{-3})	ρ_0(10 kpc) (10^{-3} g cm^{-3})	M_{hyd} ($10^{14}M_\odot$)	r_{500c} (kpc)	M_g ($10^{13}M_\odot$)
A2465 NE	337 ± 45	0.85 ± 0.11	1.578 ± 0003	9.0 ± 3.3	$1.85^{+0.60}_{-0.40}$	696^{+75}_{-50}	$1.90^{+0.05}_{-0.04}$
A2465 SW	62 ± 11	0.54 ± 0.03	10.763 ± 0.002	18.5 ± 3.1	2.17 ± 0.22	731 ± 25	0.96 ± 0.03

Table 3
Temperature Measurements in A2465

Component	r (kpc)	kT (keV)	Component	r (kpc)	kT (keV)
NE core	0–134	$3.38^{+0.42}_{-0.28}$	SW core	0–77	$2.77^{+0.21}_{-0.18}$
NE periphery	134–326	$3.55^{+0.46}_{-0.41}$	SW periphery	77–287	$2.48^{+0.24}_{-0.23}$

The $M_{hyd}(<r)$ is used to obtain r_{500c} from

$$M_{hyd}(<r_{500c}) = 500\rho_c(4\pi/3)r^3_{500c}. \quad (4)$$

Table 2 gives the best-fitting parameters for M_{hyd}, M_g, r_c, and β from the combined data plus the central values of the electron density and the mass density. Figure 4 shows the resulting enclosed gas mass profiles for the two subclusters. Within r_{500c}, the two clusters have nearly equal M_{hyd}. The NE cluster has the higher gas content ($\sim 2 \times M_g/M_{hyd}$) due to its larger core radius and at r_{200c} it has the stronger L_X and M_{200c}.

2.4. Gas Temperatures in A2465

The gas temperature of the subclusters could only be extracted near their centers. With *Chandra*, about 1800 net counts were collected from each subcluster. For the NE subcluster, a circle (0–35) arcsec corresponding to (0–134) kpc was used; the corresponding area for the SW component was (0–20) arcsec or (0–77) kpc. Data in the 0.6–10 keV band were fit to an APEC single temperature model (Smith et al. 2001). The metallicity was assumed to be $0.3\,Z_\odot$. The absorption correction was obtained from the N_H value from radio surveys (Dickey & Lockman 1990). The central temperatures are given in Table 3. Noting the difference in their brightness profiles, the NE subcluster has the higher temperature indicative of a non-cool core, while the lower temperature of the more centrally concentrated SW component suggests a cool core.

2.5. Search for Inter-component Gas and Surface Brightness Jump

Enhanced gas density or surface brightness jumps between the components of A2465 would be clues about the dynamical state of the merger. We constructed a surface brightness profile between the subclusters using the 0.5–2.0 keV *Chandra* image to maximize S/N employing the PROFFIT software package (Eckert et al. 2011). Boxes projected on the sky were 150×30 arcsec with a 45° position angle and span both subclusters including regions beyond them. The surface brightness profile in Figure 5 reveals a hot gas distribution virtually identical in both directions, with no large enhancement visible between the two subclusters. No statistically significant sharp surface

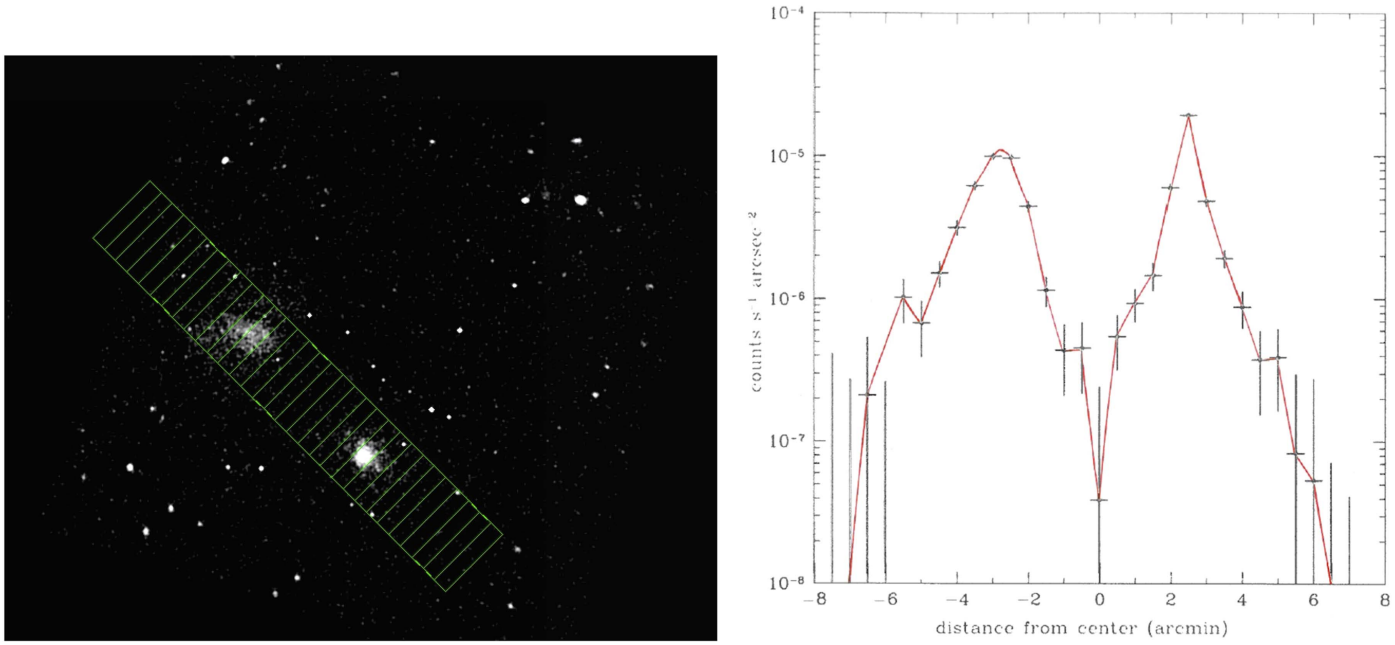

Figure 5. Showing the absence of gas enhancement and sharp intensity jumps between the components of A2465. Left: locations of bins on the *Chandra* (0.5–2.0) keV image; bins are 150 × 30 arcmins. Right: surface brightness in the bins; NE subcluster is to the left and SW to the right. The peaks are 5.25 arcmin or 1.2 Mpc apart.

brightness (or density) jumps between the two clumps were detected and no hint of elevated brightness between them, compared to the cluster outskirts, are detected at the signal to noise of the current data. We carry out a quantitative analysis using numerical simulations in Section 4.

2.6. Entropy of the Two Subclusters

The entropy provides information on a galaxy cluster's history (e.g., Voit et al. 2005; McDonald et al. 2013; Andrade-Santos et al. 2015). Here, the entropy is limited to the central regions, within radii 0–20 arcsec (or ∼68 kpc). Due to our limited data, we must emphasize the uncertainty of the resulting conclusions here.

The specific entropy is $K = kT/n_e^{2/3}$, with k as the Boltzmann constant, T as the intercluster gas temperature, and n_e as the electron density. For the NE component, $K = 78 \pm 21$ keV cm^2 and $K = 40 \pm 5$ keV cm^2 for the SW. Given that the uncertainty in these K estimates could be as much as a factor of two larger, these results are regarded as speculative. For the SW subcluster, K is consistent for a $T \sim 3$ keV relaxed cluster (Voit et al. 2005; Cavagnolo et al. 2009; McDonald et al. 2013), but for the NE component it is ∼2 times higher.

For purely gravitational heating, the reduced entropy relation is (Pratt et al. 2010)

$$K/K_{500c} = 1.42(r/r_{500c})^{1.1}, \quad (5)$$

where $K_{500c} = 106[(M_{500c}/10^{14}\,M_\odot)/f_b/E(z)]^{\frac{2}{3}}$ KeV cm^{-2}. For both components, $M_{500c} \approx 2 \times 10^{14}\,M_\odot$ with baryon fraction $f_b \approx 0.15$, $r_{500c} \approx 0.7$ Mpc, and $E(z) = 1.131$, $K_{500} \approx 550$ keV cm^2. Pratt et al. (2010) showed that K/K_{500c} divides the clusters roughly into two types, which places the SW clump ($K/K_{500c} \sim 0.07$) among cool-core clusters while the NE ($K/K_{500c} \sim 0.14$) lies with disturbed clusters. That the NE clump may still be merging is consistent with the discusion above.

Galaxy mergers, AGN activity, or subcluster mergers with core ellipticals can provide heating and raise the entropy (Seigar et al. 2003; Wang et al. 2004). A shock wave might raise K for A2465 NE. The initial K_i to final K_f ratio gives the order of magnitude of the Mach number, $M = u/c_s$, based on the Rankine–Hugoniot jump conditions (Zel'dovich & Raizer 1967; Belsole et al. 2004; Andrade-Santos et al. 2015). If the NE component was initially relaxed, $K_i \sim 25$ keV cm^2, then $K_f/K_i \sim 1.6$ and $M \approx 3.28$. For $T \sim 3$ keV, $u \sim 2900$ km s^{-1}; compared to $(2GM_{200c}/r_{200c})^{\frac{1}{2}} \sim 3000$ km s^{-1}, the maximum collisional velocity expected for the clusters.

3. Weak-lensing Analysis

Our weak-lensing results are based on Subaru/Suprime-Cam images. The weak-lensing methodology has been described in our previous papers (see Umetsu & Broadhurst 2008; Umetsu et al. 2009, 2010, 2012, 2014, 2015; Medezinski et al. 2013, 2016). We therefore refer the reader to these papers and briefly outline the methodology here.

In this work, we study the projected mass distribution in the field of A2465, $\kappa(\boldsymbol{\theta}) = \Sigma(\boldsymbol{\theta})/\Sigma_c$, which describes the projected mass density $\Sigma(\boldsymbol{\theta})$ in units of the critical surface density for lensing, $\Sigma_c = (c^2 D_s)/(4\pi G D_l D_{ls}) = c^2/(4\pi G D_l \beta)$, where D_l, D_s, and D_{ls} are the angular diameter distances to the lens, the source, and the lens-source, respectively; $\beta(z, z_l)$ is the geometric lensing strength as a function of source redshift z and lens redshift z_l.

The complex gravitational shear field $\gamma(\boldsymbol{\theta})$ is non-locally related to the convergence by $\partial^*\partial\kappa(\boldsymbol{\theta}) = \partial^*\partial^*\gamma(\boldsymbol{\theta})$, where $\partial \coloneqq \partial/\partial\theta_1 + i\partial/\partial\theta_2$ is a complex gradient operator that transforms as a vector, $\partial' = \partial e^{i\phi}$, with ϕ as the angle of rotation. In the subcritical regime where $(1-\kappa)^2 - |\gamma|^2 > 0$, the reduced gravitational shear $g(\boldsymbol{\theta}) = \gamma(\boldsymbol{\theta})/[1-\kappa(\boldsymbol{\theta})](<1)$ can be directly observed from a local ensemble of image ellipticities of background galaxies (e.g., Bartelmann & Schneider 2001).

Table 4
Optical Imaging Data of A2465

Telescope	Filter	Exposure time (s)	Seeing (arcsec)	$m_{\rm lim}$ (AB mag)	Obs. Date yyyy dd mm
Subaru/S-Cam	V	7800	0.5	27.7	2006/08/26
Subaru/S-Cam	i'	3557	0.7	26.6	2006/08/25–26
Subaru/S-Cam	z'	4720	0.8	26.5	2006/08/26
CFHT/MegaCam	g'	2060	0.9	26.1	2011/05/09
CFHT/MegaCam	r'	1500	1.0	25.4	2009/17/09
CFHT/MegaCam	i'	1895	0.5	25.5	2009/23/09

In our weak-lensing analysis of the A2465 field, we calculate the weighted average of reduced shear on a regular Cartesian grid of cells ($m = 1, 2, \ldots, N_{\rm cell}$) as

$$\langle g(\boldsymbol{\theta}_m)\rangle = \frac{\sum_i S_i(\boldsymbol{\theta}_m - \boldsymbol{\theta}_i) w_i g_i}{\sum_i S_i(\boldsymbol{\theta}_m - \boldsymbol{\theta}_i) w_i}, \quad (6)$$

where $S(\boldsymbol{\theta})$ is a spatial window function, g_i is the estimate for the reduced shear of the ith galaxy at θ_i, and w_i is the statistical weight for the ith galaxy,

$$w_i = \frac{1}{\sigma^2_{g,i} + \alpha^2_g}, \quad (7)$$

with $\sigma^2_{g,i}$ as the error variance of g_i and α^2_g as the softening constant variance taken to be $\alpha_g = 0.4$, which is a typical value of the mean rms $\sqrt{\overline{\sigma^2}_g}$ found in Subaru observations (e.g., Umetsu et al. 2009, 2014; Okabe et al. 2010; Okabe & Smith 2016). Here, the softening (α_g) is introduced so that the weight factor w_i does not span an inflated range, which could otherwise lead to an extremely unbalanced weighting. The variance of the grid reduced shear is estimated by (Umetsu et al. 2009, 2015)

$$\sigma^2_g(\boldsymbol{\theta}_m) = \frac{\sum_i S^2(\boldsymbol{\theta}_m - \boldsymbol{\theta}_i) w_i^2 \sigma^2_{g,i}}{\left(\sum_i S(\boldsymbol{\theta}_m - \boldsymbol{\theta}_i) w_i\right)^2}. \quad (8)$$

3.1. Observational Data and Photometry

For the weak-lensing analysis, we use archived imaging from the Suprime-Cam ($34' \times 27'$; Miyazaki et al. 2002) at the prime focus of the 8.3 m Subaru telescope, where archived images were obtained from SMOKA.[6] We also included observations from the CFHT/MegaCam. The CFHT/MegaCam i' and r' images have been described in Paper I and also archived.

The imaging data are summarized in Table 4. The reduction procedure is based on Nonino et al. (2009) and further described in detail by Medezinski et al. (2013). We note that the present analysis used the CFHT imaging only for the catalog making and magnitude zero-point calibration. The CFHT images were used to provide more points in defining the SED for the photo-z catalog creation and magnitude zero-point calibrations. For the weak-lensing selection and analysis, only the Subaru images were used.

Catalogs of objects in the images were extracted from the available MegaCam and Suprime-Cam images. The photometric zero points were derived using the SExtractor program (Bertin & Arnouts 1996) by matching with stars in a range of magnitude and full width half maximum (FWHM). For the CFHT images, g', r', and i' data from the Sloan Digital Sky Survey (SDSS) Data Release Nine (DR9) were used (Ahn et al. 2012). For Subaru images, z' zero points were estimated from SDSS DR9, i' employed the corrected CFHT i' imaging above, and V used data from Pickles & Depagne (2010).

For the star–galaxy separation, a plot of FWHM versus MAG_AUTO was made to locate where the point sources lie and then followed by a plot of FLUX_RADIUS versus MAG_AUTO, further finalizing the selection. The MAG_APER was computed for $\sim 1''$ FWHM and an aperture correction was derived from point sources to ~5–10 times FWHM and used to recover flux inside 1 FWHM lost due to point-spread function (psf) effects.

3.2. Shape Measurements

For shape measurements, we follow the methods of Umetsu et al. (2010, 2012, 2014, 2016). Our weak-lensing shape analysis uses the procedures of Umetsu et al. (2014; Section 4) employed for the CLASH survey. Briefly summarizing, the analysis procedures include (see also Section 3 of Umetsu et al. 2016): (1) object detection using the IMCAT peak finder, HFINDPEAKS, (2) careful close-pair rejection to reduce the crowding and deblending effects, and (3) shear calibration developed by Umetsu et al. (2010). We include for each galaxy a shear calibration factor of $1/0.95$ to account for the residual correction estimated using simulated Subaru/Suprime-Cam images. To measure the shapes of the background galaxies, we use the Subaru i' data, which have the best image quality among our data, in terms of the stability and coherence of the psf-anisotropy pattern, and were taken in fairly good seeing conditions (Table 4).

3.3. Background Selection

The background selection is critical for the weak-lensing analysis because contamination by unlensed cluster members will dilute the signal, particularly at small cluster radii (Medezinski et al. 2010; Okabe et al. 2010).

The Subaru $(i' - z') - (V - i')$ two-color diagram used for the selection of the background galaxies is shown in Figure 6, following the background selection method in Medezinski et al. (2010, 2013, 2016) and detailed in Medezinski et al. (2010). Selected background galaxies are shown by their respective blue and red colors. The region occupied by the spectroscopic sample of cluster members is outlined by the black dashed curve and the cluster member region is green.

The background sample contains 9198 (blue + red) source galaxies, corresponding to the mean surface number density of $\overline{n}_g \simeq 15$ galaxies arcmin^{-2}. We estimate the mean depths $\langle\beta\rangle$ of the blue and red background samples, which are needed when converting the measured lensing signal into physical mass units. To this end, we rely on accurate photometric redshifts

[6] http://smoka.nao.ac.jp

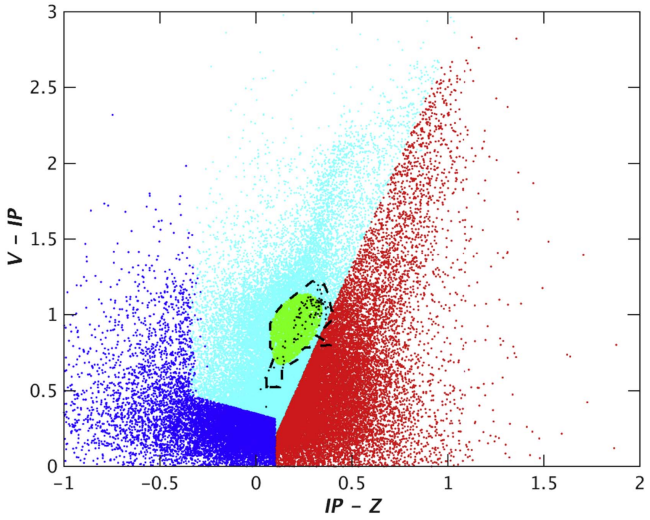

Figure 6. Showing the selection of background galaxies for the WL analysis, using Subaru V, i', and z' color–color selection. "Blue" galaxies are lower left and "red" galaxies are lower right. Rejected galaxies are shown as cyan. Black dots represent spectroscopically measured cluster members. Galaxies at small cluster-centric radius, outlined by dashes and colored green, have been excluded from the analysis.

derived for COSMOS (Capak et al. 2007) by Ilbert et al. (2009) using 30 bands in the ultraviolet to mid-infrared. We apply the same color–color/magnitude limits as for A2465 on the COSMOS catalog. However, since COSMOS photometric redshifts are reliable only to a magnitude of $\lesssim$25, whereas Subaru is deep to $\lesssim$25.4, we limit the redshift estimation to $z < 4$, and to magnitude $z' < 25$, and extrapolate the relation between depth and magnitude $\langle\beta\rangle(z')$ further from $25 < z' < 26$. Using COSMOS, we calculate the depth of each sample, red and blue, separately. Finally, we derive the mean value taking into account the relative fraction of red and blue galaxies of the total Subaru red+blue sample. For the composite blue+red sample, we find $\langle\beta\rangle = 0.7130 \pm 0.036$, corresponding to an effective source redshift of $z_{\rm eff} \simeq 1.06$.

For weak-lensing mapmaking, we draw a looser background sample, comprised of all the galaxies outside the region defined by the spectroscopic members (dashed black curves). This sample has a mean source density of $\overline{n}_g \simeq 28$ galaxies arcmin^{-2}, which is about 90% higher than that of the stringent background selection.

In Figure 7, we show a Subaru $Vi'z'$ composite image of the cluster field, produced using the publicly available TRILOGY

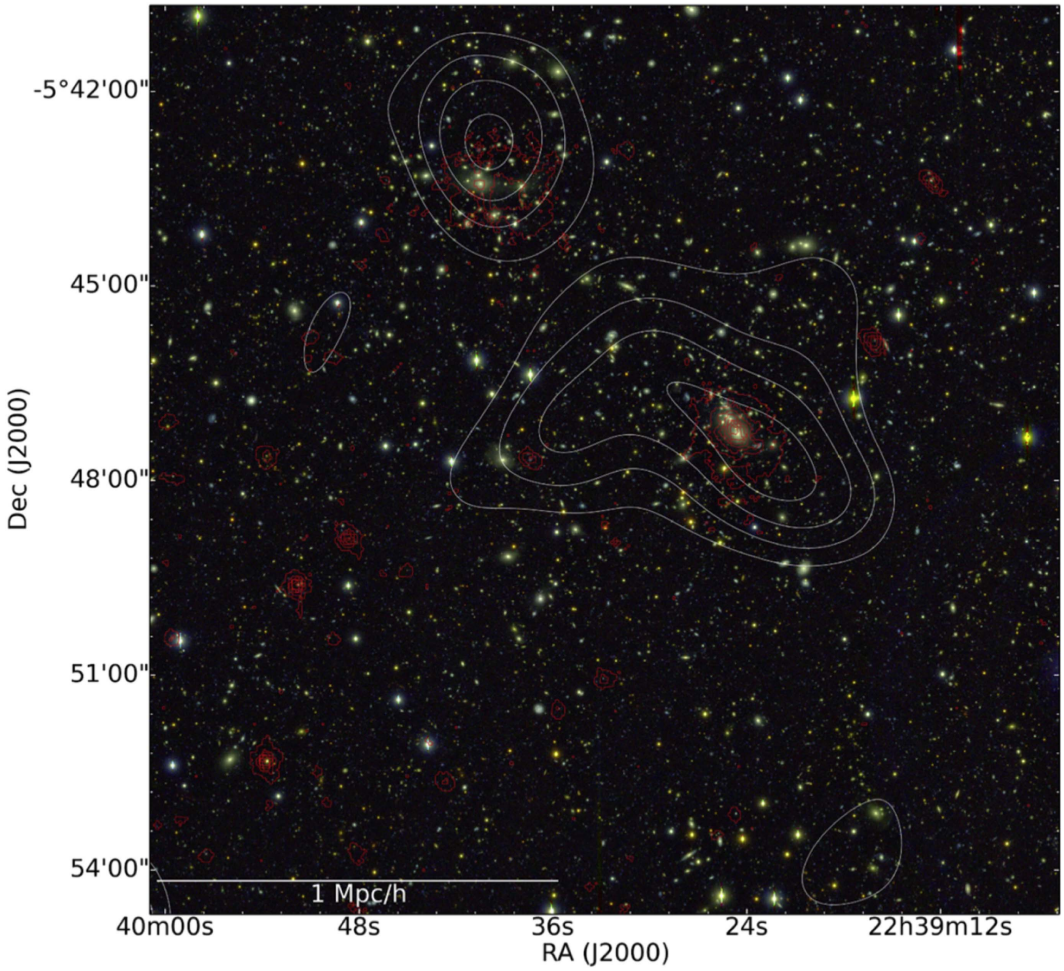

Figure 7. Subaru $Vi'z'$ composite color image in the field of A2465, overlaid with weak-lensing mass contours. The mass map is smoothed with a 2′ FWHM. The lowest contour is at the 2σ reconstruction error level ($\kappa = 0.034$) and the contour interval is $\Delta\kappa = 0.017$. The image is $14' \times 14'$ in size. The horizontal bar represents 1 Mpc h^{-1} at the cluster redshift of $z_{\rm l} = 0.245$. The red contours show the smoothed *Chandra* X-ray brightness data. North is up and east to the left.

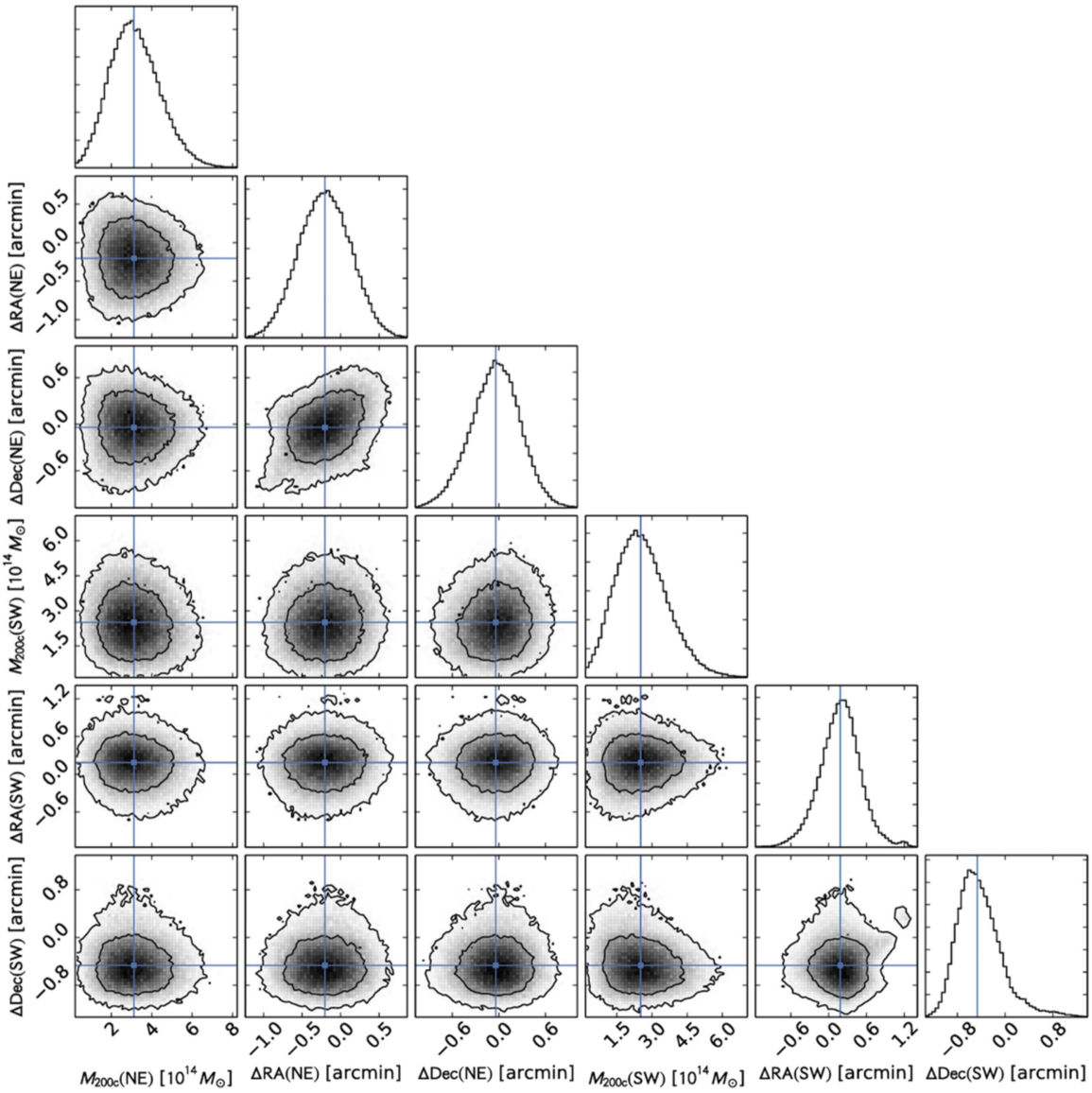

Figure 8. Posterior distributions of the NFW model parameters for the NE and SW components of A2465, obtained from multi-halo fitting to the two-dimensional Subaru reduced-shear field. For each parameter, the blue solid line shows the biweight central location of the marginalized one-dimensional posterior distribution. For each component, the halo centroid (ΔR.A., ΔDecl.) is measured relative to its brightest galaxy position.

software (Coe et al. 2012). The image is $14' \times 14'$ in size and is overlaid by Gaussian-smoothed ($2'$ FWHM) weak-lensing mass contours for visualization purposes. Here we used the Gaussian smoothing kernel as a filter function $S(\boldsymbol{\theta})$ in Equation (6).

The SW mass distribution appears pulled out along the line joining the centers of the two components. Such elongation would be consistent with tidal interaction between the two subclusters. In Paper I, the corresponding light distributions were examined. While the SW component has a sharp peak, it also seems to have an extended underlying distribution of faint galaxies and its luminosity function was found to have more galaxies with $M_I \gtrsim 20$ mag.

We note that we use this sample only for visualization purposes because it suffers from some degree of dilution. We will use the stringent (blue + red) background sample when fitting the multi-halo model to the two-dimensional shear data to find masses of the sub-structures (Section 3.4). Furthermore, unlensed foreground galaxies tend to have large photo-z biases due to inherent degeneracies stemming from finite-band determination of the photo-zs, thus diluting the weak-lensing signal.

3.4. Weak-lensing Multi-halo Mass Modeling

We perform a two-dimensional shear fitting (Okabe et al. 2011; Watanabe et al. 2011; Umetsu et al. 2012; Medezinski et al. 2013, 2016) by simultaneously modeling the two components of A2465 as a composite of two spherical halos.

To do this, we construct pixelized maps of the two-dimensional reduced-shear $g(\boldsymbol{\theta})$ (Equation (6)) and its error variance $\sigma_g(\boldsymbol{\theta})$ (Equation (8)) on a Cartesian grid of 20×24 independent cells ($N_{\rm cell} = 480$) with $0.'75$ spacing. Here we have adopted bin averaging, corresponding to $S = 1$ in Equation (6). Our multi-halo modeling is restricted to a central region with $15' \times 18'$ that contains the NE and SW components. To avoid systematic errors, we have excluded from our analysis the innermost cells lying at $|\boldsymbol{\theta}| < 1'$ from each of the halos (Oguri et al. 2010; Umetsu et al. 2012), where the surface-mass density can be close to or greater

Table 5
Offsets of Sub-component Peaks in A2465 Relative to their BCGs (arcminutes)

Component	X-ray	WL	Opt. (i')	Radio
$\Delta\alpha$ (NE)	−0.4	-0.2 ± 0.7	−0.7	0.0
$\Delta\delta$ (NE)	0.0	$+0.6 \pm 0.7$	−0.2	0.0
$\Delta\alpha$ (SW)	+0.1	-0.5 ± 1.1	0.0	…
$\Delta\delta$ (SW)	0.0	-0.4 ± 0.7	+0.5	…

than the critical value, to minimize contamination by unlensed cluster member galaxies (Section 3.3) as well as to avoid the inclusion of strongly lensed background galaxies.

We adopt the Navarro–Frenk–White (hereafter NFW; Navarro et al. 1997) model to describe the mass distribution of each cluster component. The NFW density profile provides a good description of the observed mass distribution in the intracluster regime, at least in an ensemble-average sense (e.g., Umetsu et al. 2011a, 2011b, 2014, 2016; Okabe et al. 2013; Niikura et al. 2015; Okabe & Smith 2016). We specify the NFW model using the halo mass M_{200c}, concentration $c_{200c} = r_{200c}/r_{-2}$ with r_{-2} as the characteristic radius at which the logarithmic density slope is -2, and the centroid position on the sky.

We adopt an uninformative log-uniform prior in the halo-mass interval, $0.1 \leqslant M_{200c}/(10^{14}\,M_\odot\,h^{-1}) \leqslant 100$. We set the concentration parameter for each halo using the theoretical concentration–mass relation of Dutton & Macciò (2014), which is calibrated using a *Planck* cosmology and is in good agreement with recent cluster lensing observations (Okabe & Smith 2016; Umetsu et al. 2016). For the halo centroid, we assume a Gaussian prior centered on each of the BCG positions with standard deviation $\sigma = 0.'5$ (FWHM $= 1.'18$). Accordingly, each of the NFW halos is specified by three model parameters (M_{200c}, ΔR.A., Δdecl.) where the centroid (ΔR.A., Δdecl.) is defined relative to the BCG position.

We use the Markov Chain Monte Carlo algorithm with Metropolis–Hastings sampling to constrain the multi-halo lens model from a simultaneous six-component fitting to the reduced-shear field $g(\boldsymbol{\theta})$. We employ the shear log-likelihood function of Umetsu et al. (2012; Appendix A.2) and Umetsu et al. (2016).

The marginalized posterior distributions for the multi-halo model are shown in Figure 8. The resulting constraints on the halo masses are summarized as follows:

1. $M_{200c}(\mathrm{NE}) = (3.1 \pm 1.2) \times 10^{14}\,M_\odot$ ($c_{200c} = 4.40 \pm 0.17$),
2. $M_{200c}(\mathrm{SW}) = (2.5 \pm 1.1) \times 10^{14}\,M_\odot$ ($c_{200c} = 4.49 \pm 0.20$),

where we employ the robust biweight estimators (e.g., Beers et al. 1990) for the central location (mean) and scale (standard deviation) of the marginalized posterior distributions (e.g., Sereno & Umetsu 2011; Umetsu et al. 2014) in order to reduce the contribution from outliers in the tails of the distributions. The resulting weak-lensing mass estimates are noisy with about 40% uncertainty. The mass ratio between the SW and NE halos is constrained as $M_{200c}(\mathrm{SW})/M_{200c}(\mathrm{NE}) = 0.82 \pm 0.51$. At the virial overdensity, we find

1. $M_{\rm vir}(\mathrm{NE}) = (3.7 \pm 1.5) \times 10^{14}\,M_\odot$ ($c_{\rm vir} = 5.46 \pm 0.21$),
2. $M_{\rm vir}(\mathrm{SW}) = (2.9 \pm 1.3) \times 10^{14}\,M_\odot$ ($c_{\rm vir} = 5.57 \pm 0.24$).

These can be compared with the virial masses found in Paper I, which are $(4.1 \pm 0.8) \times 10^{14} M_\odot$ and $(3.8 \pm 0.8) \times 10^{14} M_\odot$, respectively. In Table 2 from the X-ray data, the masses are similar within the errors: $M_{\rm hyd}(\mathrm{SW}) = (2.2 \pm 0.2) \times 10^{14}\,M_\odot$ but $M_{\rm hyd}(\mathrm{NE}) = (1.85^{+0.6}_{-0.4}) \times 10^{14}\,M_\odot$ is somewhat lower than the other estimates.

Along the line joining the NE and SW subclusters, the offsets of the peaks of the X-ray distributions in Figure 7 are about 0.9 and 0.7 arcmin (or ∼0.2 Mpc) closer together than the weak-lensing peaks. Relative to the BCGs, the weak-lensing offsets are smaller, being about 0.5 arcmin and consistent within the observational errors (Table 5) estimated from 100 bootstrap resampling of the background sample used for our weak-lensing mapmaking, whereas the distances of the X-ray are about half of this value. A comparison of the offsets for the optical, radio, and X-rays is in Table 5.

4. The Dynamical State of A2465

4.1. Radial Infall Model

The radial infall model (Beers et al. 1982) is discussed in Paper I. Two mass points of total mass, M, are bound if $V_r^2 R_{\rm p} \leqslant 2GM \sin^2\phi \cos\phi$. With $V_r = 205$ km s^{-1} (Paper I), A2465 satisfies this condition. Three possible solutions depend on inclination, ϕ, maximum orbital separation, $R_{\rm m}$, the system's age, t_0, assumed to be the age of the universe at redshift, z, and the development parameter, η. The observed projected distance between the masses centers is $R_{\rm p} = R\cos\phi$ and the observed velocity difference is $V_r = V \sin\phi$.

Using $M = 8 \pm 1 \times 10^{14}\,M_\odot$, $R_{\rm p} = 1.265$ Mpc, and $t_0 = 10.895$ Gyr in Paper I, the three solutions are

1. $\eta = 5.17$ rad, $\phi = 5.^\circ95$, $R = 1.31$ Mpc, $R_{\rm m} = 4.53$ Mpc, $V = -1978$ km s^{-1},
2. $\eta = 3.53$ rad, $\phi = 77.^\circ5$, $R = 6.01$ Mpc, $R_{\rm m} = 6.07$ Mpc, $V = -210$ km s^{-1},
3. $\eta = 2.68$ rad, $\phi = 81.^\circ3$, $R = 8.59$ Mpc, $R_{\rm m} = 8.81$ Mpc, $V = +208$ km s^{-1}.

Solution (3) has the subclusters moving apart and approaching maximum separation was favored in Paper I, but given the discussion here, that NE and SW have not yet collided, the other two now seem more likely. According to solutions (1) and (2), a core passage would occur in 0.4 or 6.6 Gyr, respectively. Possibly solution (1) is preferable in light of the enhanced star formation induced by the higher impact velocity.

We estimate the probability of the system being bound for the three solutions ($i = 1, 2, 3$). Using the upper and lower limits on the inclination, ϕ_1 and ϕ_2 from $V_r = 205 \pm 149$ km s^{-1} shown in Figure 18 of Paper I, we calculate the probability, P_i (e.g., Beers et al. 1982; Andrade-Santos et al. 2015), from the relative probabilities, $p_i = \int_{\phi_1}^{\phi_2} \cos\phi d\phi$, normalized by $P_i = p_i/\Sigma_i p_i$. This yields

$$P_1 = 85\%,\ P_2 = 12\%,\ \text{and}\ P_3 = 3\%,$$

which favors the infalling solutions over the separating one.

4.2. Modeling the Interaction

For more detailed modeling, we follow Molnar et al. (2013), who analyzed the A1750 double cluster. This employs the FLASH program, which is a parallel Eulerian code originating from the Center for Astrophysical Thermonuclear

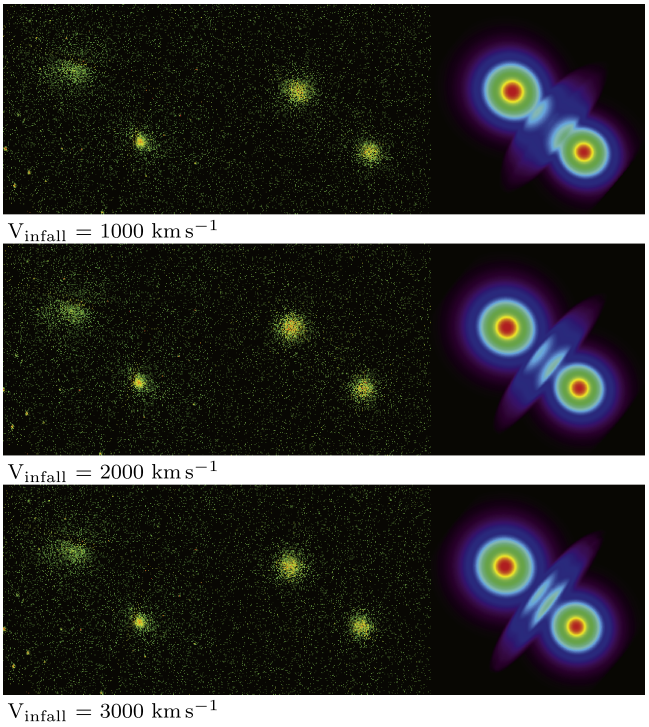

Figure 9. Examples of simulated X-ray observations based on our FLASH simulations with different infall velocities as marked (V_{infall}; top to bottom) for A2465 compared with *Chandra* observations. From left to right: image from *Chandra* observations; mock X-ray observation fitted to the *Chandra* flux; model X-ray surface brightness.

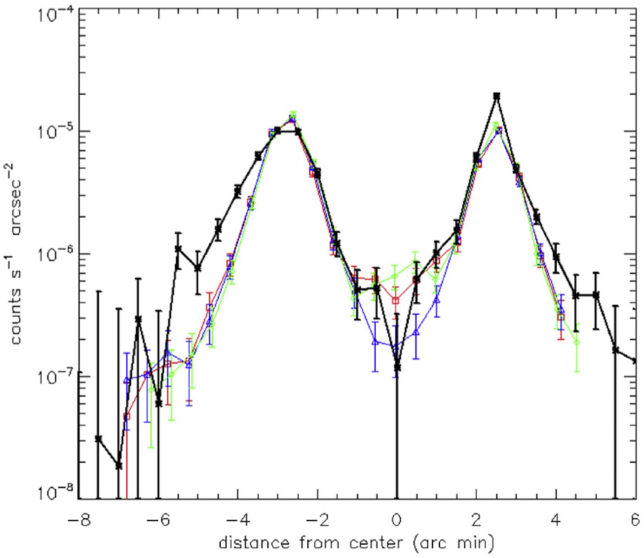

Figure 10. X-ray surface brightness profiles along the line connecting the two X-ray peaks from *Chandra* observations (stars with error bars connected with thick black solid lines), from mock observations with $V_{infall} = 1000$ and 2000 km s^{-1} (red squares and green diamonds with error bars connected with solid lines of the same color; presented in Figure 9), and from mock observations assuming that the clusters are not interacting, they look close to each other only in projection (blue triangles with error bars).

Flashes at the University of Chicago (Fryxell et al. 2000; Ricker 2008). Further details of the binary merger models are given in Molnar et al. (2012). Briefly, the dark matter and galaxies are modeled by truncated NFW profiles and β models are used for the gas. The velocities are taken to be isotropic and follow the relations in Lokas & Mamon (2001). Similar modeling has been conducted extensively for other clusters, e.g., the "Bullet" cluster, the best studied post-merger, using different programs (see Lage & Farrar 2014, 2015).

In simulating the A2465 system, we assumed masses $M_{vir,1} = 4 \times 10^{14} M_{\odot}$ and $M_{vir,2} = 3 \times 10^{14}\, M_{\odot}$ and concentration parameters $c_{vir,1} = 5$ and $c_{vir,2} = 6$, which are consistent with the weak-lensing measurements in Section 3.4. We ran FLASH simulations with a range of collisional velocities V_{infall} and impact parameters P. We generated mock X-ray observations based on our simulations choosing the phase of the collision that matches the observations and adding noise similar to that of the *Chandra* observations of A2465. The results presented here are relevant to our study of the dynamical state of A2465. Models with $V_{infall} =$ 1000, 2000, and 3000 km s^{-1} and $P = 150$ kpc are shown in Figure 9 (top to bottom). In this figure we show cluster X-ray surface brightness distribution (no noise) based on our FLASH simulations, images of mock *Chandra* observations (noise added), and, for comparison, the X-ray image from our *Chandra* observation (left to right). It can be seen from the X-ray surface brightness distribution (right panels) that the morphology of the emission changes as a function of infall velocity. The two X-ray peaks associated with the shock/compression heated intracluster gas of the two components are closer to the centers of the colliding clusters for lower infall velocities. Unfortunately the depth of the X-ray observations is insufficiently deep enough to see the detailed morphology of the interaction region.

Solutions (2) and (3) imply that the two clusters appear close to each other due to a projection effect; they are actually 6 and 8.59 Mpc apart, and the collision is close to the LOS ($\phi = 77.^{\circ}5$ and $\phi = 81.^{\circ}3$). In this case, no enhanced X-ray emission should be observed between the two cluster centers, just a simple superposition of their equilibrium gas emission.

Solution (1) of our simplified dynamical analysis suggests that the collision is close to the plane of the sky, $\phi = 5.^{\circ}95$, and the intracluster gas of the two components are already interacting (in collision), since $R = 1.31$ Mpc is less than the sum of the two virial radii. In this case, we should see enhanced X-ray emission from the shock/compression heated intracluster gas between the two cluster centers. In solution (1), the 3D relative velocity between the subclusters is $V = -1978$ km s^{-1}. Our simulations with infall velocities of $V_{infall} = 1000$ km s^{-1} and 2000 km s^{-1} bracket this value (note that the infalling cluster speeds up as it falls in, so its infall velocity should be slightly less than $V = -1978$ km s^{-1}). Note that at this large distance, $R \geqslant 1.3$ Mpc, the relative velocity of the infalling cluster is insensitive to the expected impact parameter ($P \lesssim 300$ kpc), since it is moving in the shallow outer part of the cluster's gravitational potential.

Consequently we extract data from our mock images based on our FLASH simulations assuming $V_{infall} = 1000$ km s^{-1} and 2000 km s^{-1} from the same regions in the sky used for our *Chandra* analysis (shown in Figure 5) and derive the X-ray profiles along the line between the two X-ray peaks. In Figure 10 we compare the surface brightness profile between the two cluster centers extracted from our *Chandra* observations (stars with error bars connected with black thick solid line) and the profiles extracted from our mock observations based on simulations with $V_{infall} = 1000$ km s^{-1} and 2000 km s^{-1} (red

squares and green diamonds with error bars connected with solid lines of the same color; same data were used in Figure 9). Triangles with error bars connected with a blue solid line represent an X-ray profile assuming no interaction between the two clusters (corresponding to solutions (2) and (3)).

As it can be seen from Figure 10, the simulations predict an enhancement between the two X-ray peaks if there is a collision in progress. The enhancement in the X-ray data seems to be significant between the two cluster centers even with the low exposure time assumed for the image simulations. Based on a likelihood analysis using a χ^2 statistic and restricting the fitting to the relevant region (between the cluster centers), we obtain $\chi^2 = 56$, 63, and 88 (with nine degrees of freedom) for our models with $V_{\rm infall} = 1000$ km s^{-1}, 2000 km s^{-1}, and the non-interacting model (marked red, green, and blue in Figure 10). Our best-fit model has $V_{\rm infall} = 1000$ km s^{-1}. Based on the reduced $\Delta\chi^2$ values relative to this model, the non-interacting model can be excluded with 90% CL (confidence level). The model with $V_{\rm infall} = 2000$ km s^{-1} can only be excluded in favor of the best-fit model with less than 68% CL. We conclude that the X-ray observations are not deep enough to obtain meaningful constraints on the infall velocity of the less massive subcluster, but the non-merging case can be excluded with 90% CL. Thus, our simulations suggest that A2465 is in a process of collision, the intracluster gas of the two components are already interacting, but we cannot constrain the infall velocity of the system using only our FLASH simulations.

5. Discussion

There are numerous examples of double and multiple merging galaxy clusters, discovered and analyzed in recent years with which to compare A2465. These objects provide information on galaxy formation and evolution, give clues on the interactions of the clusters' baryonic and dark matter interactions, as well as the behavior of gravitation on megaparsec scales. The interactions of different types of dark matter through pressure effects (Ota & Yoshida 2016), dynamical friction, and self-interacting dark matter (Irshad et al. 2014; Kahlhoefer et al. 2014) or modified gravity (e.g., Del Popolo 2013; Matsakos & Diaferio 2016) could, in principle, produce observable effects. Since the subclusters are separated by about 1.2 Mpc, the substantial overlap of their halos suggests possible interaction between the two components.

Although promising, analysis of double clusters has proven difficult because in many cases their geometry is complex and interacting systems range from pre-mergers, given in the Introduction (Okabe & Umetsu 2008; Andrade-Santos et al. 2015), as well as the A3407+A3408 pair (Nascimento et al. 2016) to post-core passage objects, many of which also show complicated structures. The $\sim 2 \times 10^{15} M_{\odot}$ "El Gordo" cluster (Jee et al. 2014, 2016) only shows one X-ray peak, CIZA J2242.8+5301, which is highly elongated (Jee et al. 2015), and CIZA J0107.7+5408 (Randall et al. 2016), which is a complex dissociative merger.

Using the basic properties of the two subcomponents in A2465 derived above and in Papers I and II, scaling relations for single galaxy clusters indicate nothing unusual. Both components follow the cluster M_{200c}–L_X relations (e.g., Reiprich & Böhringer 2002; Rykoff et al. 2008) and the T_X–M_{200c} relations (e.g., Popesso et al. 2005). However, enhanced star formation was found in Paper II. The SW subcluster appears to have a lower than normal gas fraction, $f_{\rm gas} = M_{\rm gas}/M_{\rm hyd}$. From Table 2, $f_{\rm gas} = 0.10$ for the NE subcluster, and it is 0.04 for the SW component. In the $f_{\rm gas}$–T_X relations in Sanderson et al. (2003), Vikhlinin et al. (2006), Sun et al. (2009), Sun (2012),Gonzales et al. (2013), and Lovisari et al. (2015), the corresponding gas fractions are about 0.10.

The NVSS radio data (Paper I) give $P_{1.4} = 1.1 \times 10^{24}$ WHz^{-1} for the NE component of A2465 and with $L_X = 9 \times 10^{43}$ erg s^{-1}, it places it among the low X-ray clusters in the (L_X, $P_{1.4}$) relation for radio halos (Feretti et al. 2012). One possibly comparable object in this class is A523 (Giovannini et al. 2011), which is considered to be a merger. Other mergers do not host a radio halo, like the case of the SW component.

The reduced entropies for the centers of each subcluster seem to agree with these conclusions. For the SW component, $K/K_{500c} \approx 0.07$ is in the range for cool-core or gravitationally collapsed clusters (e.g., Pratt et al. 2010) and the higher value ($K/K_{500c} \approx 0.14$) for the NE could be attributed to a morphologically disturbed cluster due to a separate earlier merging event rather than interaction with the SW. Due to our limited data, this should only be considered indicative rather than conclusive.

The low exposure time of our X-ray observations of A2465 does not allow a quantitative dynamical analysis based on N-body/hydrodynamical simulations. The infall velocity, impact parameter, etc. of the system cannot be derived, but combining the simplified dynamical analysis with the FLASH simulations allows us to find an approximate dynamical state of the system, specifically, to distinguish between a non-interacting system and one in an early state of merging. Our FLASH simulations suggest enhanced X-ray emission between the two cluster centers (relative to assuming a simple superposition of the two equilibrium cluster emission), which can be attributed to shock/compression heated intracluster gas due to merging. We have found only one solution, applying our simplified dynamical analysis, which results in a stage of merging, close to solution (1) of the radial infall model with a 3D relative velocity of $V = -1978$ km s^{-1} between the clusters and a 3D distance of $R = 1.31$ Mpc. Our FLASH simulations cannot constrain the relative velocity (or the infall velocity) alone, but they indicate a pre-core passage state for the cluster.

From these data it appears that the NE and SW components of A2465 resemble the nearer and somewhat less massive double cluster A3716 (PLCKG345.40-39.34) studied by Andrade-Santos et al. (2015), who concluded that that cluster is in a pre-collisional state, and the binary clusters A1750 and A1758 (Okabe & Umetsu 2008), which also appear to be in the early merger stages. Consequently A2465 is an excellent candidate for studying the early stages of galaxy cluster collisions.

Physical separation of the galaxy, gas, and dark matter components has been modeled by many investigators with different theories of dark matter and gravity (e.g., Lage & Farrar 2015; Massey et al. 2015; Schaller et al. 2015; Kim et al. 2017). For A2465, the small separations are near the limits of reliability of our data. The offsets relative to the BCGs of each subcluster (using the positions of the BCGs in Table 1 of Paper I) are in Table 5. For comparison, the scale on the sky at A2465 is 0.23 Mpc arcmin^{-1} and the NE and SW subcluster BCGs are at a projected distance of 5.25 arcmin or 1.2 Mpc. The subcomponents in Table 5 lie roughly along the projected line connecting the BCGs in each subcluster. If we take the

midpoint of this line as the cluster center, the X-ray peaks lie closer to this center and the weak-lensing peaks are farther apart. The small ∼0.2 Mpc weak-lensing to X-ray separations (which can be seen in Figure 7) are less than in, e.g., the "Bullet" cluster (Clowe et al. 2006), but are comparable to some other clusters. Given the 1.7 arcmin smoothing of the weak-lensing, the offsets are uncertain and the situation is unclear. Also in the pre-merger state, the gas is expected to trail the galaxies and dark matter. Simulations of merging halos (e.g., by Vijayaragharan & Ricker 2015) show the stripped gas trails and galaxy wakes that would follow rather than precede the subclusters.

It is of note that although the weak-lensing and optical data assign the higher mass to the NE sub-component, from weak lensing it has a more symmetrical profile of mass contours. The SW sub-component with the more compact central region has more unsymmetrical and extended outer mass contours that show a flattened shape perpendicular to the line joining the two subclusters. This might be a sign of the merging of the two components.

The total SFR normalized to the cluster mass, $\sum \mathrm{SFR}/M_{\mathrm{cl}}$, in galaxy clusters has been studied by several authors (Paper II contains a partial list). In Paper II, it was found that A2465 NE and SW lie above the mean redshift z and M_{cl} relations. Although additional data for mergers in different dynamical states show large scatter, lower M_{cl} systems tend to have higher SFR efficiencies. In post-merger systems, recent mergers tend to have higher SFR, while it is reduced in more evolved mergers (Laganá et al. 2008; Sobral et al. 2015; Stroe et al. 2015b). These results are still based on a small number of systems, but a plausible picture is shock-induced star formation. Early in a merger, shocks produce increased star formation in the gas-rich galaxies, leading to rapid gas consumption, which exhausts the star formation phase. Heating from the merger increasingly quenches the SFR for massive systems and significant amounts of the gas are pushed from the cluster center by feedback from supernovae and/or active galaxies (e.g., Zhang et al. 2011). The A2465 system could fit into this picture as it is a pre-merger that has not lost its gas content and still has a high SFR.

6. Conclusions

The goal of this investigation was to determine the dynamical state of the components of the double galaxy cluster A2465. In advanced mergers these are known to separate. The X-ray data reveal the distribution of the baryonic gas component and the weak lensing shows the distribution of the total mass including dark matter. This can be compared with the distributions of the luminous matter from Papers I and II. From this study we draw the following conclusions.

(1) Using the *Chandra* X-ray observations in Section 2.1, the X-ray surface profiles of the NE and SW components were fit employing modified β models. The NE subcluster has a broader profile than the SW component. The *Chandra* X-ray data provided temperatures, gas and total masses, and gas fractions, and determined a central entropy. This indicates that the NE and SW subclusters have gas masses 1.90 and $0.96 \times 10^{13}\,M_{\odot}$ and total masses 1.85 and $2.17 \times 10^{14}\,M_{\odot}$.

(2) The entropy profiles from the X-ray data differ for the two subclusters. The NE central entropy is higher than the SW. The NE could have undergone a recent merger. This seems consistent its three BCGs and radio halo. The SW subcluster is more relaxed as it has a sharper central profile, suggestive of a cool core.

(3) Section 2.5 shows that there are no large amounts of X-ray gas between the two subclusters of A2465, such as are found in post-merger colliding clusters, e.g., the "Bullet" cluster.

(4) The weak-lensing analysis in Section 3 utilizes Subaru Suprime-Cam $Vi'z'$ images. A two-dimensional shear fitting with simultaneous modeling of the two components of A2465 was conducted. The weak-lensing virial masses are 3.7 and $2.9 \times 10^{14}\,M_{\odot}$ compared to 4 and $3 \times 10^{14}\,M_{\odot}$ from redshift data (Paper I). The cluster as a whole is of an intermediate mass ($M \lesssim 10^{15}\,M_{\odot}$). The projected mass contours in Figure 7 show some distortion, but only small offsets between them and the X-ray gas.

(5) From the optical redshift measurements in Paper I, the two subclusters of A2465 should be gravitationally bound. The absence of strong X-ray emission between the two subcomponents and lack of large offsets between the galaxies and weak-lensing centers suggest that the two subclusters have not yet collided (i.e pre-core passage). The probabilities of the system being bound for the three possible solutions in Section 4.1 and the likelihood analysis in Section 4.2 strengthen the pre-merger case. The FLASH simulations and radial infall model indicate that they will meet in ∼0.4 Gyr.

(6) The enhanced normalized star formation, $\sum \mathrm{SFR}/M_{\mathrm{cl}}$, found in Paper II and that A2465 is a pre-merger could be consistent with a shock-induced star formation process using gas that has not yet been driven from the system by the merger.

It seems clear that the NE and SW components of A2465 are in a pre-merger state. Although there is no large separation of the collisionless and baryonic components, such a system might help provide constraints on their interactions as they merge. Future observations that could better determine the orbital parameters would be useful for detailed dynamical modeling.

The *Chandra* observations were supported by NASA grant GO2-13150A to G.A.W., who wishes to acknowledge correspondence on A2465 from Ryan Johnson, Catherine Heymans, Eric Tittley, Meghan Gray, David Helfand, Robert Becker, Adi Zitrin, Emilio Falco, Ho Seong Hwang, and William Dawson. K.U. acknowledges support by the Ministry of Science and Technology of Taiwan through grants *MOST* 103-2112-M-001-030-MY3 and *MOST* 103-2112-M-001-003-MY3. W.F. and C.J. acknowledge support from the Smithsonian Astrophysical Observatory and contract NAS8-03060 from NASA. M.N. acknowledges support from PRIN-INAF 2014 1.05.01.94.02. This work is based in part on data collected at the Subaru Telescope and obtained from the Subaru-Mitaka-Okayama-Kiso-Archive (SMOKA), which is operated by the Astronomy Data Center, National Astronomical Observatory of Japan (Baba et al. 2002). We thank the anonymous referee for comments that improved this paper.

References

Abell, G. O. 1958, ApJS, 3, 211
Ahn, C. P., Alexandroff, R., Allende, P., et al. 2012, ApJS, 203, 21
Andrade-Santos, F., Jones, C., Forman, W. R., et al. 2015, ApJ, 803, 108
Baba, H., Yasuda, N., Ichikawa, S.-I., et al. 2002, in ASP Conf. Ser. 281, Astronomical Data Analysis Software and Systems XI, ed. D. A. Bohlender, D. Durand, & T. H. Handley (San Francisco, CA: ASP), 298
Bartelmann, M., & Schneider, P. 2001, PhR, 340, 291

Beers, T. C., Flynn, K., & Gebhardt, K. 1990, AJ, 100, 32
Beers, T. C., Geller, M. J., & Huchra, J. P. 1982, ApJ, 257, 23
Belsole, E., Pratt, G. W., Sauvageot, J.-L., et al. 2004, A&A, 415, 821
Bertin, E., & Arnouts, S. 1996, A&AS, 117, 393
Bradač, M., Allen, S. W., Treu, T., et al. 2008a, ApJ, 687, 959
Bradač, M., Schrabback, T., Erben, T., et al. 2008b, ApJ, 681, 187
Capak, P., Aussel, H., Ajik, M., et al. 2007, ApJS, 172, 99
Cavagnolo, K. W., Donahue, M., Voit, G. M., & Sun, M. 2009, ApJS, 182, 12
Clowe, D., Bradač, M., Gonzales, A. H., et al. 2006, ApJ, 648, 109
Coe, D., Umetsu, K., Zitrin, A., et al. 2012, ApJ, 757, 22
Cohen, S. A., Hickox, R. C., Wegner, G. A., Einasto, M., & Vennik, J. 2014, ApJ, 783, 136
Condon, J. J., Cotton, E. W., Griesen, E. W., et al. 1998, AJ, 115, 1693
Dawson, W. A., Wittman, D., Jee, M., et al. 2012, ApJL, 747, L42
Del Popolo, A. 2013, in AIP Conf. Ser. 1548, IX Mexican School on Gravitation and Mathematical Physics, ed. L. A. Urena-Lopez, R. Becerril-Barcenas, & R. Linares-Romero (Melville, NY: AIP), 2D
Dickey, J. M., & Lockman, F. J. 1990, ARA&A, 28, 215
Dutton, A. A., & Macciò, A. V. 2014, MNRAS, 441, 3359
Eckert, D., Molendi, S., & Paltani, S. 2011, A&A, 526, 79
Feretti, L., Giovannini, D., Govoni, E., & Murgia, M. 2012, A&ARv, 20, 54
Fryxell, B., Olson, K., Ricker, P., et al. 2000, ApJS, 131, 273
Giovannini, G., Feretti, L., Girardi, M., et al. 2011, A&A, 530, L5
Gonzales, A. H., Sivanandam, S., Zabludoff, A. I., & Zaritsky, D. 2013, ApJ, 778, 14
Helfand, D. I., White, R. L., & Becker, R. H. 2015, ApJ, 801, 26
Hwang, H. S., & Lee, M. G. 2009, MNRAS, 397, 2111
Ilbert, O., Capak, P., Salvato, M., et al. 2009, ApJ, 690, 1236
Irshad, M., Liesenborgs, J., Saha, P., & Williams, L. L. R. 2014, MNRAS, 439, 2651
Jee, M. J., Dawson, W. A., Stroe, A., et al. 2016, ApJ, 817, 179
Jee, M. J., Hughes, J. P., Menanteau, F., et al. 2014, ApJ, 785, 20
Jee, M. J., Stroe, A., Dawson, W., et al. 2015, ApJ, 802, 46
Kahlhoefer, F., Schmidt-Hoberg, K., Frandsen, M. T., & Sarkar, S. 2014, MNRAS, 437, 2865
Kim, S. Y., Peter, A. H. G., & Wittman, D. 2017, MNRAS, 469, 1414
Kitayama, T., & Suto, Y. 1996, ApJ, 469, 480
Laganá, T. F., Neto, G. B. F., Andrade-Santos, F., & Cypriano, E. S. 2008, A&A, 485, 633
Lage, C., & Farrar, G. R. 2014, ApJ, 787, 144
Lage, C., & Farrar, G. R. 2015, JCAP, 02, 038
Lokas, E. L., & Mamon, G. A. 2001, MNRAS, 321, 155
Lovisari, L., Reiprich, T. H., & Schellenberger, G. 2015, A&A, 573, 118
Markevitch, M., & Vikhlinin, A. 2007, PhR, 443, 1
Massey, R., Williams, L., Smit, R., et al. 2015, MNRAS, 449, 3393
Matsakos, T., & Diaferio, A. 2016, JCAP, submitted (arXiv:1603.04943)
McDonald, M., Benson, B. A., & Vikhlinin, A. 2013, ApJ, 774, 23
Medezinski, E., Broadhurst, T., Umetsu, K., et al. 2010, MNRAS, 405, 257
Medezinski, E., Umetsu, K., Nonino, M., et al. 2013, ApJ, 777, 43
Medezinski, E., Umetsu, K., Okabe, N., et al. 2016, ApJ, 817, 24
Merten, J., Coe, D., Dupke, R., et al. 2011, MNRAS, 417, 333
Miyazaki, S., Komiyama, Y., Sekiguchi, M., et al. 2002, PASJ, 54, 833
Molnar, S. M., Chiu, I.-N. T., Broadhurst, T., & Stadel, J. G. 2013, ApJ, 779, 63
Molnar, S. M., Hearn, S. C., & Stadel, J. G. 2012, ApJ, 748, 45
Nascimento, R. S., Ribeiro, A. L. B., Trevisan, M., et al. 2016, MNRAS, 460, 2193
Navarro, J. F., Frenk, C. S., & White, S. D. M. 1997, ApJ, 490, 493
Niikura, H., Takada, M., Okabe, N., Martino, R., & Takahashi, R. 2015, PASJ, 67, 103
Nonino, M., Dickinson, M., Rosati, P., et al. 2009, ApJS, 183, 244
Oguri, M., Takada, M., Okabe, N., & Smith, G. P. 2010, MNRAS, 405, 2215
Okabe, N., Bourdin, H., Mazzotta, P., & Maurogordato, S. 2011, ApJ, 741, 116
Okabe, N., & Smith, G. P. 2016, MNRAS, 461, 3794
Okabe, N., Smith, G. P., Umetsu, K., Takada, M., & Futamase, T. 2013, ApJL, 769, L35
Okabe, N., Takada, M., Umetsu, K., et al. 2010, PASJ, 62, 811
Okabe, N., & Umetsu, K. 2008, PASJ, 60, 345
Ota, N., & Yoshida, H. 2016, PASJ, 68, 19
Owers, M. S., Randall, S. W., Nulsen, P. E. J., et al. 2011, ApJ, 728, 27
Perlman, E., Horner, D. J., Jones, L. R., et al. 2002, ApJS, 140, 265
Pickles, A. J., & Depagne, É 2010, PASP, 122, 1437
Poole, G. B., Fardal, M. A., Babul, A., et al. 2006, MNRAS, 373, 881
Popesso, P., Biviano, A., Bohringer, H., Romaniello, M., & Voges, W. 2005, A&A, 433, 431
Pratt, G. W., Arnaud, M., Piffaretti, R., et al. 2010, A&A, 511, 85
Randall, S. W., Clarke, T. E., van Weeren, R. J., et al. 2016, ApJ, 823, 94
Randall, S. W., Markevitch, M., Clowe, D., Gonzales, A. H., & Bradač, M. 2008, ApJ, 679, 1173
Reiprich, T., & Böhringer, H. 2002, ApJ, 567, 716
Ricker, P. M. 2008, ApJS, 176, 293
Ricker, P. M., & Sarazin, C. L. 2001, ApJ, 561, 621
Roettiger, K., Loken, C., & Burns, J. O. 1997, ApJS, 109, 307
Russell, H. R., McNamara, B. R., Sanders, J. S., et al. 2012, MNRAS, 423, 236
Rykoff, E. S., Evrard, A. E., McKay, T. A., et al. 2008, MNRAS, 387, 28
Sanderson, A. J. R., Ponman, T. J., Finoguenov, A., & Lloyd-Davies, E. J. 2003, MNRAS, 340, 989
Sarazin, C. L. 1986, RvMP, 58, 1
Schaller, M., Robertson, A., Massey, R., Bower, R. G., & Eke, R. G. 2015, MNRAS, 453, L58
Seigar, M. S., Lynam, P. D., & Chorney, N. E. 2003, MNRAS, 344, 110
Sereno, M., & Umetsu, K. 2011, MNRAS, 416, 3187
Smith, R. K., Brickhouse, N. S., Liedahl, D. A., & Raymond, J. C. 2001, ApJL, 556, L91
Sobral, D., Stroe, A., Dawson, W. A., et al. 2015, MNRAS, 450, 630
Spergel, D. N., & Steinhardt, P. J. 2000, PhRvL, 84, 3760
Stroe, A., Oosterloo, T., Rottgering, H. J. A., et al. 2015a, MNRAS, 452, 2731
Stroe, A., Sobral, D., Dawson, W., et al. 2015b, MNRAS, 450, 646
Sun, M. 2012, NJPh, 14, 5004S
Sun, M., Voit, G. M., Donahue, M., et al. 2009, ApJ, 693, 1142
Takizawa, M. 2000, ApJ, 532, 183
Umetsu, K., Birkinshaw, M., Liu, G.-C., et al. 2009, ApJ, 694, 1643
Umetsu, K., & Broadhurst, T. 2008, ApJ, 684, 177
Umetsu, K., Broadhurst, T., Zitrin, A., Medezinski, E., & Hsu, L.-Y. 2011a, ApJ, 729, 127
Umetsu, K., Broadhurst, T., Zitrin, A., et al. 2011b, ApJ, 738, 41
Umetsu, K., Medezinski, E., Broadhurst, T., et al. 2010, ApJ, 714, 1470
Umetsu, K., Medezinski, E., Nonino, M., et al. 2012, ApJ, 755, 56
Umetsu, K., Medezinski, E., Nonino, M., et al. 2014, ApJ, 795, 163
Umetsu, K., Sereno, M., Medezinski, E., et al. 2015, ApJ, 806, 207
Umetsu, K., Zitrin, A., Gruen, D., et al. 2016, ApJ, 821, 116
Vijayaraghavan, R., & Ricker, P. M. 2013, MNRAS, 435, 2713
Vijayaraghavan, R., & Ricker, P. M. 2015, MNRAS, 449, 2312
Vikhlinin, A., Kravtsov, A., Forman, W., et al. 2006, ApJ, 640, 691
Vikhlinin, A., Markevitch, M., Murray, S. S., et al. 2005, ApJ, 628, 655
Vikhlinin, A., McNamara, B. R., Forman, W., et al. 1998, ApJ, 502, 558
Voit, G. M., Kay, S. T., & Bryan, G. L. 2005, MNRAS, 364, 909
Wang, Q. D., Owen, F., & Ledlow, M. 2004, ApJ, 611, 821
Watanabe, E., Takizawa, M., Nakazawa, K., et al. 2011, PASJ, 63, 357
Wegner, G. A. 2011, MNRAS, 413, 1333
Wegner, G. A., Chu, D. S., & Hwang, H. S. 2015, MNRAS, 447, 1126
Zel'dovich, Ya. A., & Raizer, Yu. P. 1967, in Physics of Shock Waves and High-temperature Hydrodynamic Phenomena, ed. W. D. Hayes & R. F. Probstein (New York: Academic Press)
Zhang, Y.-Y., Laganá, T. F., Pierini, D., et al. 2011, A&A, 535, 78